




RESEARCH ARTICLE

Tumor-associated astrocytes promote tumor progression of Sonic Hedgehog medulloblastoma by secreting lipocalin-2

Haishuang Li^{1,2,3}  | Yuqing Liu²  | Yantao Liu^{1,2,3} | Luzheng Xu⁴ |
 Ziwen Sun^{1,2,3} | Danfeng Zheng^{1,3} | Xiaodan Liu^{1,3} | Chen Song⁵ | Yu Zhang⁵ |
 Hui Liang¹ | Bao Yang⁶ | Xinxia Tian¹ | Jianyuan Luo^{5,7} | Qing Chang^{2,3} 

¹Department of Pathology, School of Basic Medical Sciences, Peking University Third Hospital, Peking University Health Science Center, Beijing, China

²Department of Neuropathology, Beijing Neurosurgical Institute, Tiantan Hospital, Capital Medical University, Beijing, China

³Beijing Key Laboratory of Research and Transformation of Biomarkers for Neurodegenerative Diseases, Peking University Third Hospital, Peking University Health Science Center, Beijing, China

⁴Department of Medical and Health Analysis Center, Peking University Health Science Center, Beijing, China

⁵Department of Medical Genetics, Center for Medical Genetics, Peking University Health Science Center, Beijing, China

⁶Department of Neurosurgery, Tiantan Hospital, Capital Medical University, Beijing, China

⁷Beijing Key Laboratory of Protein Posttranslational Modifications and Cell Function, Department of Biochemistry and Molecular Biology, Peking University Health Science Center, Beijing, China

Correspondence

Qing Chang, Department of Neuropathology, Beijing Neurosurgical Institute, Beijing Tiantan Hospital, Capital Medical University, Beijing 100070, China.

Email: changqing055@bjni.org.cn

Jianyuan Luo, Department of Medical Genetics, Center for Medical Genetics, Peking University Health Science Center, Beijing 100191, China.

Email: luojianyuan@bjmu.edu.cn

Xinxia Tian, Department of Pathology, School of Basic Medical Sciences, Peking University Third Hospital, Peking University Health Science Center, Beijing 100191, China.

Email: tianxinxia@163.com

Funding information

Beijing Health Commission Foundation, Grant/Award Number: 11000023T000002044300-4; Beijing Key Laboratory of Research and Transformation of Biomarkers for Neurodegenerative Diseases, Grant/Award Number: BZ0436; Beijing Natural Science Foundation, Grant/Award Numbers: 7192095, 7232098; National Natural Science Foundation of China, Grant/Award Numbers: 81101900, 30540008, 81972353

Abstract

Sonic Hedgehog (SHH) subgroup of medulloblastoma (MB) accounts for about 25% of all subgroups of MB. Tumor microenvironment (TME) may play a key role in the tumor progression and therapeutic resistance. Tumor-associated astrocytes (TAAs) are reshaped to drive tumor progression through multiple paracrine signals. However, the mechanism by which TAAs modulate MB cells remains elusive. Here, we illuminated that TAAs showed a specific and dynamic pattern during SHH-MB development. Most TAAs gathered to the tumor margin during the tumor progression, rather than evenly distributed in the early-stage tumors. We further demonstrated that lipocalin-2 (LCN2) secreted by TAAs could promote the tumor growth and was correlated with the poor prognosis of MB patients. Knocking down LCN2 in TAAs in vitro impeded the proliferation and migration abilities of MB cells. In addition, we identified that TAAs accelerated the tumor growth by secreting LCN2 via STAT3 signaling pathway. Accordingly, blockade of STAT3 signaling by its inhibitor WP1066 and AAV-*Lcn2* shRNA, respectively, in TAAs abrogated the effects of LCN2 on tumor progression in vitro and in vivo. In summary, we for the first time clarified that LCN2, secreted by TAAs, could promote MB tumor progression via STAT3 pathway and has potential prognostic value. Our findings unveiled a new sight in reprogramming the TME of SHH-MB and provided a potential therapeutic strategy targeting TAAs.

KEYWORDS

LCN2, medulloblastoma, tumor-associated astrocytes, tumor microenvironment

Haishuang Li and Yuqing Liu are co-first authors.

This is an open access article under the terms of the [Creative Commons Attribution-NonCommercial-NoDerivs](https://creativecommons.org/licenses/by-nc-nd/4.0/) License, which permits use and distribution in any medium, provided the original work is properly cited, the use is non-commercial and no modifications or adaptations are made.

© 2023 The Authors. *Brain Pathology* published by John Wiley & Sons Ltd on behalf of International Society of Neuropathology.

1 | INTRODUCTION

Medulloblastoma (MB) is one of the most common malignant brain tumors in children, accounting for 25%–30% [1]. At least four consensus subgroups of MB are reported in the 2021 World Health Organization classification of tumors, including wingless (WNT), Sonic Hedgehog (SHH) (with or without P53 mutation), and non-WNT/SHH (Groups 3 and 4) [2]. Different genetic signatures and DNA methylation status of each subgroup lead to different prognosis, histopathological features, and therapeutic strategy. Among them, SHH-MB accounts for about 25% of all subgroups [3], which is driven by the aberrant activation of SHH signaling pathway [4]. While a standard treatment of surgical resection, chemotherapy, and radiation has improved the overall 5-year survival rate for MB patients up to 60%–90% [5], survivors are left with life-long side effects such as endocrine dysfunction, ataxia, and irreversible brain damage [6, 7]. Many of these sequelae are caused by current aggressive therapeutic strategy. More specific and less toxic treatments are urgently needed.

There is a growing consensus that tumors should be regarded as a living organ rather than a mass composing of individual tumor cells [8]. Studies have reported that tumor microenvironment (TME) of MB plays a key role in the tumor progression and therapeutic resistance [9, 10]. Reprogramming TME to destroy the ecological support of the tumor is the effective strategy of tumor therapy. Therefore, it is imperative to get a better understanding of the mechanism of crosstalk between tumor cell and other cells in TME.

Tumor-associated astrocytes (TAAs) were considered to play a critical role in MB development [9, 11, 12]. Compared with the normal astrocytes, TAAs showed increased reactivity in the tumor [13]. The increased expression of glial fibrillary acid protein (GFAP) was regarded as a sensitive marker for reactive astrocytes [14]. Previous studies have reported that high expression of GFAP was significantly associated with poor prognosis of MB patients [15]. Recent study reported that more TAAs were recruited in the disseminated MB compared with the primary tumor caused by IL6 derived from tumor stem cells [16]. These studies implicated that the TAAs seem to have different effects during MB development. However, the dynamic change of TAAs during MB progression and the mechanisms by which TAAs were activated to support tumor growth were largely unknown.

Herein, we performed differentially expressed genes (DEGs) analysis in TAAs and identified lipocalin-2 (LCN2) as a critical biomarker related to MB tumorigenesis. LCN2, also known as neutrophil gelatinase-associated lipocalin (NGAL) belongs to the lipocalin protein family which transports small hydrophobic molecules such as steroids, retinoids, and lipids [17]. Previous studies indicated that the expression of LCN2 could be detected in reactive astrocyte, activated microglia,

neuron, as well as endothelial cell under neuropathological state rather than in normal brain tissue [18–20]. In brain tumors, the biological function of LCN2 protein remains controversial. It was reported that LCN2 expression level was negatively correlated with the clinical outcome of glioma [21]. While deletion of LCN2 in glioma cells contributed to chemoresistance [22]. A recent study reported that LCN2 secreted by endothelial cell was up-regulated by tumor-derived exosome in glioma [23]. However, it still remains unclear the functions of LCN2 in the tumor progression of MB.

In this study, we explored the function of TAAs of SHH-MB in mouse model and co-culture system. We identified for the first time that LCN2 secreted by TAAs promoted the tumor growth via the JAK2/STAT3 signaling pathway. Our findings unveiled a new sight in reprogramming the TME of SHH-MB and provided a potential target for TAAs-based antitumor therapy.

2 | MATERIALS AND METHODS

2.1 | Cell culture

Human Daoy and D341 MB cell line were kindly provided by Prof. Ho Ho-Keung Ng of The Chinese University of Hong Kong. Human ONS-76 MB cell line was kindly provided by Prof. Xiu-Wu Bian of Southwest Hospital of Army Medical University. Daoy and ONS-76 were cultured in Dulbecco's Modified Eagle's Medium (DMEM) supplemented with 10% fetal bovine serum (FBS), streptomycin, and penicillin. D341 was cultured in Minimum Essential Medium containing 20% FBS.

2.2 | Isolation of primary mouse astrocytes

Primary astrocytes were isolated from newborn C57 mice according to the previous study [24]. Briefly, after disinfecting in 75% alcohol, take the brain in precooled F12/DMEM and carefully strip away the meninges. The brain tissue was then cut into homogenate with a sterile surgical blade and resuspended with precooled F12/DMEM, taking care not to damage the cells. Filter the homogenate through a 75- μ m filter into a 50-mL tube, and centrifuge for 6 min at 4°C, 1500 rpm. The pellets were resuspended with F12/DMEM containing 10% FBS, 1% penicillin/streptomycin, 1% L-glutamin, 1% sodium pyruvate, and 1% nonessential amino acid. Cells were cultured in T75 flasks, and the medium were changed every 3 days. All cells were kept at 37°C in a cell incubator containing 5% CO₂.

2.3 | Transgenic mice

ND2SmoA1 transgenic mice were purchased from Jackson Labs (#008831) and approved by the Department of

Laboratory Animal Science of Peking University [10]. All animal experiments were performed in accordance with institution guidelines of the Peking University Institutional Animal Care and Use Committee (No. LA2019121). Mice were raised in the Department of Laboratory Animal Science of Peking University under standard conditions at room temperature and a 12-h light and dark cycle with free access to food and water.

2.4 | Magnetic resonance imaging

Three to six months of ND2-SmoA1 mice were used in this study as previously described [25]. The tumors of mice were detected by 3.0 T Siemens Trio Scanner (Siemens Healthcare Sector) with a 20-mm diameter mouse body coil. Briefly, mice were anesthetized by 2.5% isoflurane and 95% oxygen. T2-weighted 2D RARE quick scans were acquired. Echo time: 89 ms, repetition time: 5960 ms, number of averages: 4, field of view (FOV): 6.4 cm × 3.9 cm, matrix: 729256 × 100, 15 slices, slice thickness: 0.9 mm. Data were analyzed by Micro DICOM software.

2.5 | Animal experiments

To pharmacologically inhibit the expression of LCN2 in TAAs, the tumor-bearing mice were randomized and divided into two groups for treatment with vehicle control ($n = 9$), and WP1066 (Selleck) (20 mg/kg, intraperitoneal, $n = 9$). WP1066 is sequentially dissolved in saline containing 5% DMSO, 40% PEG300, and 5% Tween-80 to ensure clarity. WP1066 or the vehicle was administered three times a week, and the dose was adjusted with the body weight of mice. Magnetic resonance imaging (MRI) scan was performed once a week after 2 weeks of administration. The weight of mice was measured daily.

2.6 | Injection of adeno-associated viruses

Adeno-associated virus (AAV)-GFAP-eGFP viral vectors containing Mouse *Lcn2*-shRNA or scramble-shRNA (AAV PHP.eB, 1.0×10^{13} VG/ml, Genomeditech) were used in this study. AAV-*Lcn2* shRNA (AAV-sh-*Lcn2*) or AAV-scramble shRNA (AAV-scramble) was injected with a single dose of 1.0×10^{12} VG per mouse via tail vein. The target sequence of AAV for knockdown of LCN2 was designed based on the previous study [26]. The target sequences of sh-*Lcn2* and scramble were as follows: sh-*Lcn2*, 5'-CCAGTTCACCTCTGG-GAAAT-3'; scramble, 5'-TTCTCCGAACGTGT-CACGT-3'. Mice injected with AAV-sh-*Lcn2* or AAV-scramble were randomly divided into the following four groups: AAV-scramble + Vehicles ($n = 6$); AAV-scramble + Sonidegib ($n = 6$); AAV-sh-*Lcn2* + Vehicles

($n = 6$); AAV-sh-*Lcn2* + Sonidegib ($n = 5$). Sonidegib (20 mg/kg, Selleck) was dissolved in corn oil containing 2% DMSO. Sonidegib and vehicle were orally administered daily, and the dose was adjusted according to the body weight of mice. MRI scan was performed every 10 days.

2.7 | Immunofluorescence staining

ND2SmoA1 tumor-bearing mice were anesthetized with 1% sodium pentobarbital, 30 mL PBS was used for cardiac perfusion, and the brain was taken out. After being fixed in the 4% paraformaldehyde for 24 h, the brains were immersed into the 30% sucrose solution for dehydration. The sagittal brain sections (10 μ m) were prepared with a sliding microtome (Leica). Brain slices were washed with PBS and treated with blocking solution (1% BSA, 0.4% Triton X-100, and 4% goat serum in PBS) for 1 h. Next, brain slices were incubated with Rabbit monoclonal antibody IBA1 (012-26723, Wako, 1:300), Chicken monoclonal antibody GFAP (ab4674, Abcam, 1:500), Rabbit polyclonal antibody Ki67 (ab15580, Abcam, 1:500), Synaptophysin Mouse Monoclonal Antibody (67864, Proteintech, 1:250), Rabbit monoclonal antibody STAT3 (phosphorylation Y705) (ab76315, Abcam, 1:300), Mouse polyclonal antibody LCN2 (AF1857, R&D, 1:50), Rabbit polyclonal antibody SLC22A17 (NBP1-76918, NOVUS, 1:50) diluted in blocking solution overnight at 4°C. Brain slices were then washed with PBS and incubated with Goat Anti-Mouse IgG H&L (Alexa Fluor[®] 488) (ab150117, Abcam, 1:500), Goat Anti-Rabbit IgG H&L (Alexa Fluor[®] 594) (ab150079, Abcam, 1:500), Goat Anti-Rabbit IgG H&L (Alexa Fluor[®] 488) (ab150113, Abcam, 1:500), Goat Anti-Chicken IgY H&L (Alexa Fluor[®] 555) (ab150170, Abcam, 1:500) diluted in TBST for 2 h. After washing with TBST, brain slides were incubated with DAPI for 3 min. Immunofluorescence images were captured at room temperature using a Zeiss710 instrument.

2.8 | Western blot analysis

All experiments were performed on ice. Cells and the tissue sections were lysed in RIPA containing protease inhibitors and phosphatase inhibitors. Protein lysates were separated by 4%–12% sodium dodecyl sulfate polyacrylamide gel electrophoresis (P41215, LEBLEAD), and then transferred to a polyvinylidene fluoride membrane (ISEQ00010, Merck Millipore, 0.22 μ m). After blocking with 5% skimmed milk, the membrane was incubated with Rabbit polyclonal antibody LCN2 (A3176, ABClonal, 1:500), Rabbit monoclonal antibody p-STAT3 (Tyr705) (9154, CST, 1:1000), Mouse monoclonal antibody p-STAT3 (S727) (9136, CST, 1:1000), Rabbit monoclonal antibody STAT3 (4904, CST, 1:1000), Rabbit monoclonal antibody JAK2 (3230, CST, 1:1000)

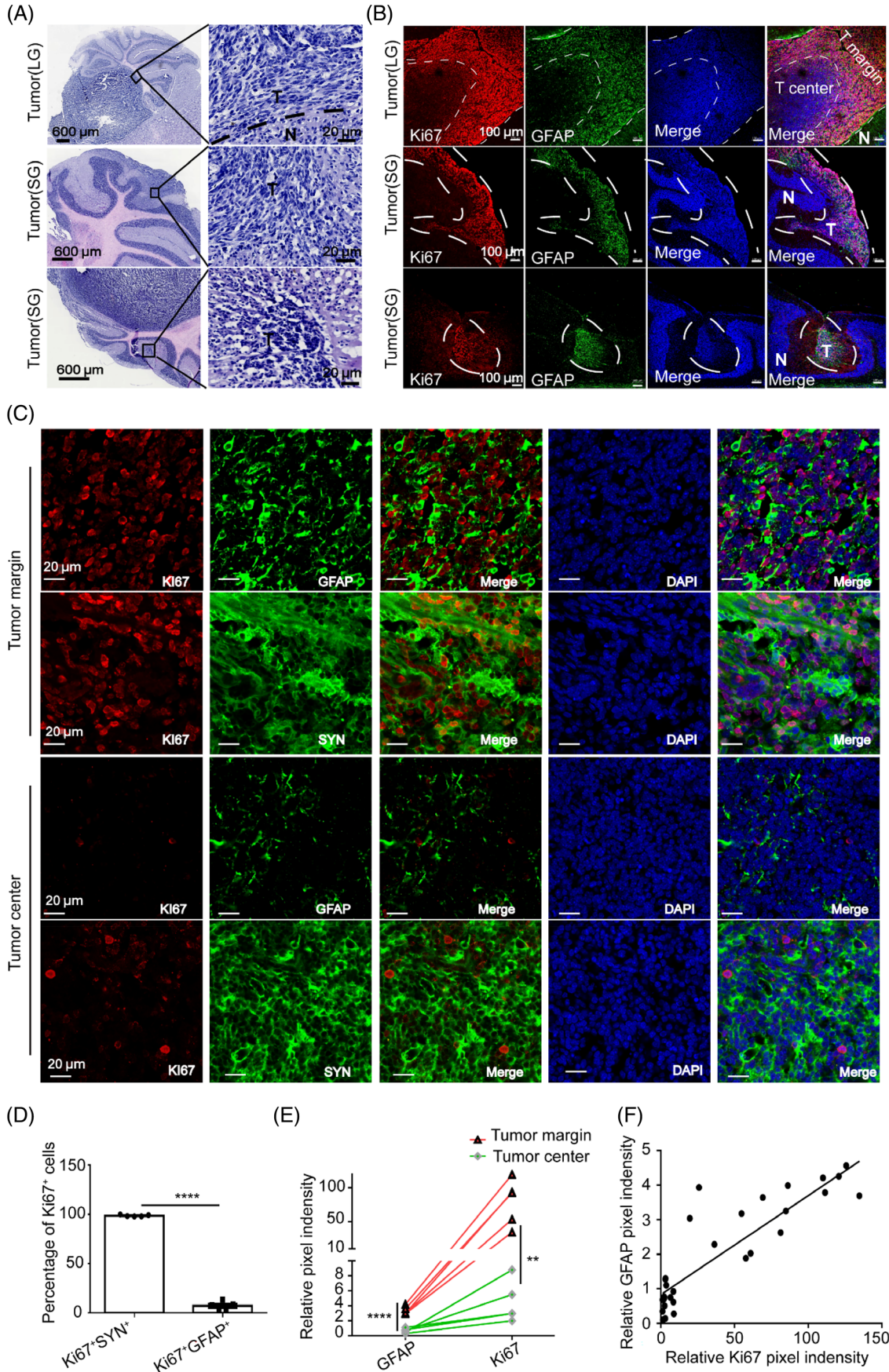


FIGURE 1 Legend on next page.

diluted in blocking solution at 4°C overnight. Then the membranes were incubated with horseradish peroxidase-conjugated secondary antibodies at room temperature for 1 h. Protein signals were visualized with Super ECL Plus Substrate (Thermo Fisher) in Gel imaging system (Bio-Rad ChemiDoc MP). ImageJ (Ver.1.53e; NIH, Bethesda, MD) was used to quantify the protein bands, normalized to β -actin, and determined as the percentage value.

2.9 | Cell studies

To detect the cell proliferation, Daoy or ONS-76 were seeded in 96 well plates at a density of 6×10^3 cells per well. Cells were cultured in 100 μ L conditional medium of normal astrocytes or TAAs and cell proliferation was measured at 12, 24, 36, and 48 h. Ten microliters of CCK8 were added to each well and incubated at 37°C for 2 h at each time point. The absorbance value at the wavelength of 450 nm was measured on microplate reader (Thermo Scientific). Trans-well assay and wound healing assay were used for migration assay as previously described [27]. All experiments were triple-repeated.

2.10 | RNA extraction and quantitative real-time PCR analysis

Total RNA was harvested from cells using TRIzol Reagent (Thermo Fisher Scientific) according to the manufacturer's protocol. Total RNA was reverse transcribed using the cDNA synthesis kit (Yeasten, 11142ES60). The resulting cDNA was used for qPCR amplification using the Universal Blue qPCR SYBR Green Master Mix (Yeasten, 11184ES08) according to the manufacturer's protocol on the CFX96 Real-Time System (Bio-Rad). The primers used can be found in Table S1.

2.11 | RNA-sequencing and bioinformatic analysis

The total RNA was obtained from normal astrocytes (ASs) and TAAs. The TAAs were induced by co-culture

with Daoy for 24 h. RNA purity was checked using the kaiaoK5500[®] Spectrophotometer (Kaiao, Beijing, China). A total amount of 2 μ g RNA per sample was used as input material for the RNA sample preparations. Sequencing libraries were generated using NEBNext[®] Ultra[™] RNA Library Prep Kit for Illumina[®] (#E7530L, NEB, USA) following the manufacturer's recommendations, and index codes were added to attribute sequences to each sample. Analysis of sequencing data by the method described previously [28]. Figures were plotted by Sangerbox (<http://www.sangerbox.com/tool>), a free online platform for data analysis and visualization [29].

2.12 | ELISA assay

The secretion of LCN2 in astrocytes was detected by Elisa Kit (DG96425Q, Dogesce) according to the instructions. Briefly, the cell supernatants were centrifuged to remove debris and polymers. The standards, samples, and HRP labeled antibody were added to the 96 well plates and incubated for 1 h at 37°C. The plates were washed, and the substrate solution was added for another 15 min at 37°C. Add stop solution to each well and read the OD value at 450 nm on the microplate reader.

2.13 | Transfection of small interfering RNA

Three candidate small interfering RNA (siRNA) targeting LCN2, and a scrambled control were designed. Astrocytes were transfected with LCN2 siRNA (siLCN2-1-3), negative control siRNA (siNC) using lipofectamine 3000 (Invitrogen, L3000-015, CA, USA) following the manufacturer's instructions. The sequences of siRNA used are listed in Table S1.

2.14 | Statistical analysis

The data are presented as the mean \pm SEM. Statistical differences between two groups were analyzed using Student's *t* test, and one-way ANOVA or two-way ANOVA were performed to compare three groups or more, except

FIGURE 1 The distribution density of tumor-associated astrocytes was correlated with tumor progression in ND2SmoA1 MB mouse model. (A) The brain slices of ND2SmoA1 mice bearing tumors with large volume (LG) and early-stage tumors with small volume (SG) were stained by HE. (B) Immunofluorescence staining of GFAP (green color) and Ki67 (red color) were performed to determine the distribution pattern of TAAs and the proliferation ability of cells in MB, respectively (T: MB tumor, N: normal cerebellum, T center: the field of view at the center of tumor, T margin: the field of view at the border between tumor and normal brain tissue). (C) The expression of SYN, GFAP, and Ki67 in tumor margin (up) and tumor center (down) were detected on tumor slides from MB mice. (D) The numbers of GFAP⁺ Ki67⁺ cells and SYN⁺ Ki67⁺ cells were counted with Photoshop software. They were then normalized by the total Ki67⁺ cell number as the percentages of the proliferation of TAAs and tumor cells in MB, respectively (five pictures were randomly captured for the tumor of each mouse, $n = 5$). (E) The immunofluorescence pixel intensity of GFAP and Ki67 in the tumor centers or tumor margins of MB in LG was quantified by ImageJ software, respectively (five pictures were randomly captured in both tumor center and tumor margin of the tumor of each mouse, $n = 5$). (F) Pearson correlation analysis between the immunofluorescence pixel intensity of GFAP and Ki67 in MB was performed (five pictures were randomly captured for the tumor of each mouse, $n = 10$, $R^2 = 0.07612$, $p < 0.0001$).

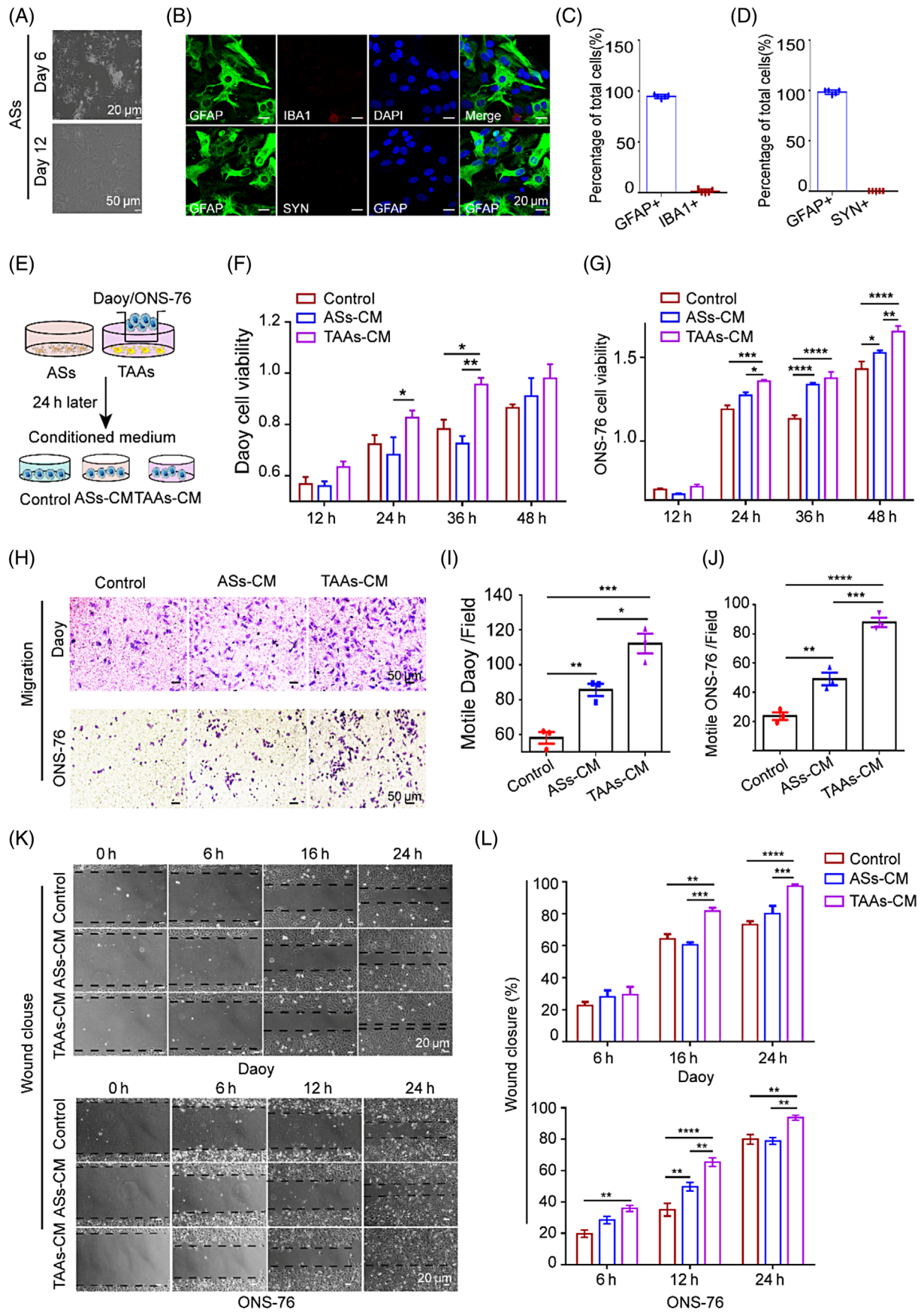


FIGURE 2 Legend on next page.

where otherwise noted. $p < 0.05$ was considered statistically significant. All statistical analyses and graphic work were performed using Prism 8.0 (GraphPad Software Inc.) and Adobe Illustrator CC 2018.

3 | RESULTS

3.1 | The distribution density of TAAs is correlated with the tumor progression in ND2-SmoA1 SHH-MB mouse model

To explore the TAAs distribution pattern during tumor progression of MB, we first detected MB transgenic mice bearing tumor at different time points by nuclear MRI. Histologic sections were then evaluated under microscope after H&E staining. Among these mice, some early-stage tumors were too small to be detected by MRI but can be observed under microscope, which were defined as the small group (SG). Those tumors with larger volumes, which can be easily identified by MRI, were defined as the large group (LG) (Figure 1A).

To further evaluate the TAAs in tumor, we detected the TAAs and MB tumor cells using glial fibrillary acidic protein (GFAP) and synaptophysin (SYN) as markers, respectively, by immunofluorescence. Ki67 was applied to indicate the proliferative capacity of cells. We found that TAAs evenly distributed in SG tumors, showing general high proliferation ability. But in LG tumors, TAAs mainly gathered at the tumor margin. Interestingly, tumor cells always exhibit significantly higher proliferation ability in regions with more TAAs. (Figure 1B, Figure S1A–D). By double staining, we confirmed the expression of Ki67 mainly concentrated in the SYN-positive tumor cells rather than GFAP-positive TAAs, indicating that the TAAs were non-proliferative (Figure 1C,D). Further quantification analysis showed that the proliferation ability of MB cells in both groups was positively correlated with the number of TAAs (Figure 1E,F). These results showed that the distribution density of TAAs was correlated with the proliferative ability of MB tumor cells, although they changed with tumor volumes. To explore whether the correlation between the tumor proliferation and the distribution pattern of TAAs was specific in MB, we further mapped the distribution of tumor-associated macrophages (TAMs) in MBs

with different sizes. Our results showed that TAMs were evenly distributed in these tumors (Figure S1E). These results suggested that the heterogeneity of tumor proliferation ability may have a more close relationship with TAAs rather than TAMs during tumor progression.

3.2 | TAAs increased the proliferation and migration ability of MB tumor cells

To confirm the relationship between TAAs and tumor growth, we evaluated whether the TAAs alone could affect the proliferation and migration ability of tumor cells using a co-culture model in vitro. First, we isolated the normal astrocytes (ASs) from the brain of C57 newborn mice. After 6–12 days of culture, ASs attached to the bottom of culture flask gradually (Figure 2A). To confirm the purity of the primary astrocytes, immunofluorescence double staining was performed. GFAP, IBA1, and SYN were used as markers for astrocytes, microglia, and neurons, respectively (Figure 2B). Most cells (94.64%–98.41%) are GFAP⁺, while only a few cells (6.73%) are IBA1⁺ (Figure 2C,D), indicating the high purity of the ASs.

To obtain TAAs in vitro, we co-cultured the primary astrocytes with Daoy or ONS-76 cells (SHH-MB) for 24 h. ASs and TAAs were cultured for another 24 h to obtain the conditioned medium, respectively (Figure 2E). The conditioned medium of TAAs significantly promoted the proliferation (Figure 2F,G) and migration (Figure 2H–L) ability of both Daoy and ONS-76, indicating that TAAs secreted some specific bio-signals into the medium and induced cell growth of SHH-MB.

3.3 | Increased LCN2 expression in TAAs is related to the poor prognosis of MB

Previous studies reported that TAAs in MB may be correlated with stemness of tumor cells in MB, especially in SHH-MB [11, 30, 31]. We identified considerable astrocytes in the tumor of ND2-SmoA1 SHH-MB mouse model, however, only a small number of cancer stem cells (0.05% of total cells in MB) were detected by flow cytometry (Figure S2). These results suggested that TAAs

FIGURE 2 Tumor-associated astrocytes promoted the proliferation and migration ability of MB cells in vitro. (A) Cell morphologies of primary normal astrocytes cultured for 6 days, and 12 days were observed by light microscope. (B) After 12 days of culture, immunofluorescence staining of GFAP, IBA1, and SYN was performed to detect the purity of the primary isolated astrocytes. (C, D) The numbers of GFAP⁺, IBA1⁺, and SYN⁺ cells were quantified and normalized to the total number of DAPI⁺ cells in each field (five views were randomly captured). (E) Illustration of workflow. To obtain TAAs in vitro, astrocytes were pre-co-cultured with Daoy or ONS-76 for 24 h. The conditioned medium of astrocytes (ASs-CM) and TAAs (TAAs-CM) were collected to treat MB cells and assess their effects on tumor cell proliferation and migration ability. The control group was treated with the normal culture medium. (F, G) CCK8 assay was performed to analyze cell viability of Daoy and ONS-76 treated by the ASs-CM or TAAs-CM. (H, K) Trans-well and wound healing assays were performed to determine cell migration ability of Daoy and ONS-76 treated by ASs-CM or TAAs-CM. The cell numbers of Daoy (I) and ONS-76 (J) that migrated were quantified. (L) The percentages of wound closure at each time point were normalized by wound area of 0 h, which were expressed as the mean \pm SEM from at least three independent experiments. Representative images were shown. p -values are determined by two-way ANOVA (F, G, L) or one-way ANOVA (I, J).

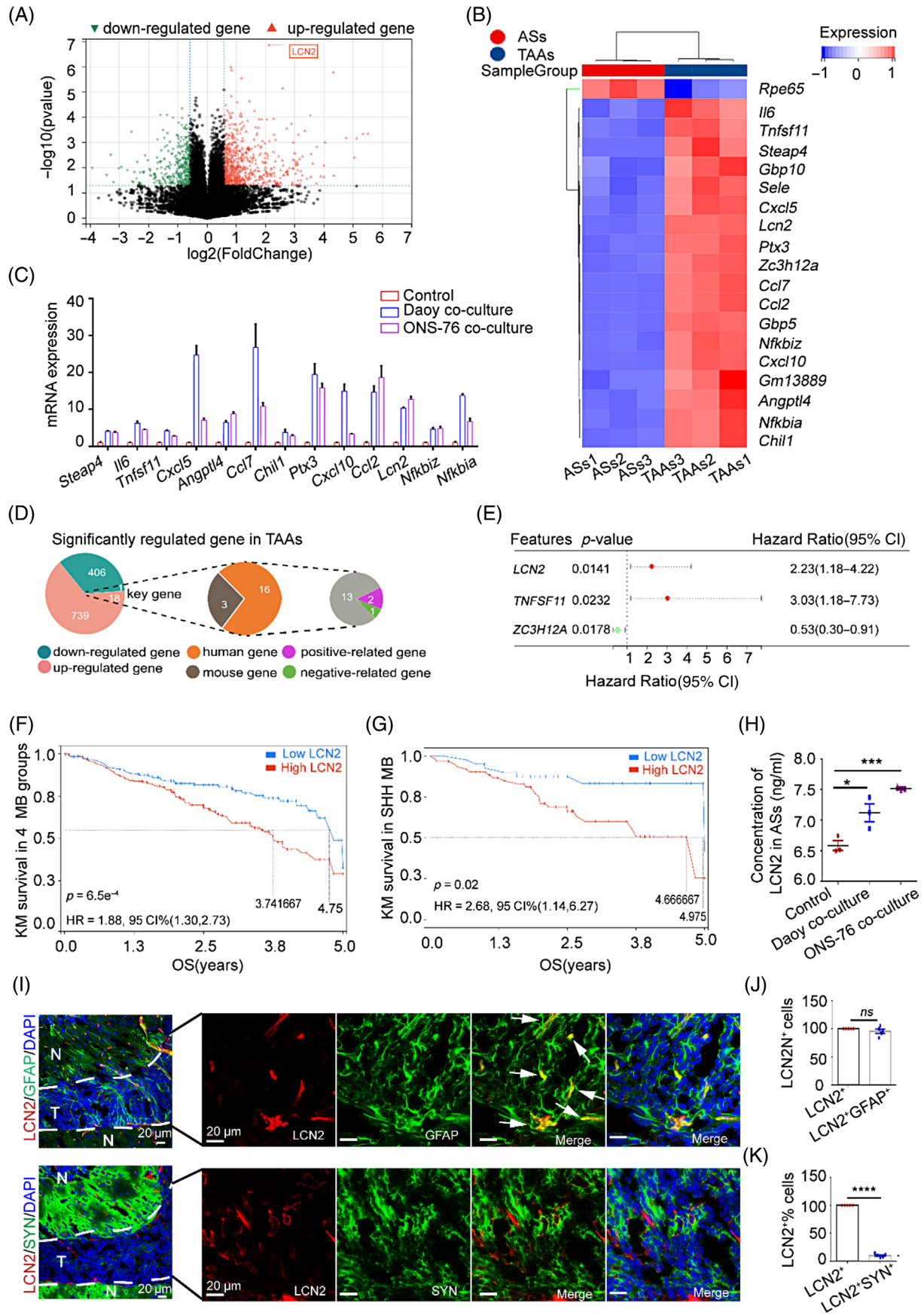


FIGURE 3 Legend on next page.

may promote the tumor progression in other ways rather than tumor stem cells in MBs.

To clarify the specific tumor-related bio-signals secreted by the TAAs, we performed differential expression analysis of TAAs by RNA sequencing assay. Totally 757 up-regulated genes and 407 down-regulated genes out of 28,891 genes were identified in TAAs compared with ASs (Figure 3A). The most significant DEGs were verified in TAAs by q-PCR (Figure 3B,C, Table S2).

To screen the genes in TAAs with clinical value, we performed a univariate Cox regression model to estimate the prognostic significance of the DEGs in TAAs based on GSE85218 dataset (Figure 3D, Table S3). The result showed that the expression of *LCN2*, *TNFSFL1*, and *ZC3H2A* were significantly related with the OS in MB patients. Among them, patients with high expression of *LCN2* and *TNFSFL1* had relatively worse prognosis (p value was 0.0141 and 0.0232, respectively), while patients with high expression of *ZC3H2A* had better prognosis ($p = 0.0178$) (Figure 3E). Compared with *TNFSFL1* ($p = 0.10$) (Figure S3A), MB patients with high expression levels of *LCN2* had a significant worse prognosis ($p = 6.5e^{-4}$) (Figure 3F). In addition, we evaluated the prognostic significance of *LCN2* in the four MB subgroups and found that high expression of *LCN2* was significantly correlated with poor prognosis of all MBs except WNT subgroup, which had relatively good prognosis in MB (Figure 3G, Figure S3B–D). The expression of *LCN2* in human MB was further validated by the immunohistochemical and immunofluorescence staining in human MB samples (Figure S3E,F). These results indicated that the high expression of *LCN2* in TAAs was associated with the poor prognosis of MB, especially in the poor-survival subgroups of MB.

As a secreted protein, *LCN2* plays a pivotal role in the crosstalk between tumor cells and other cell populations in the TME [32, 33]. In order to verify the secreted *LCN2* in TME of MB, we further performed ELISA to detect the *LCN2* secreted by TAAs. The results showed that both Daoy and ONS-76 could significantly induce the secretion of *LCN2* in TAAs in vitro (Figure 3H). To clarify whether *LCN2* is mainly generated by TAAs, we

detected the *LCN2* within TAAs and MB cells by immunofluorescence in ND2SmoA1 mice (Figure 3I). *LCN2* expression was mainly detected in GFAP⁺ TAAs rather than SYN⁺ MB cells (Figure 3J,K). However, as the main receptor of *LCN2*, *SLC22A17* expression was observed in both TAAs and MB tumor cells in MB mice (Figure S4A).

To further explore the mechanism that elevated *LCN2* promotes the proliferation and invasion of MB tumor cells, we analyzed the expression profiling of A549 stimulated with *LCN2* protein based on GSE54962 dataset [34]. Totally, 3838 DEGs were categorized based on KEGG pathway, molecular function, cellular component, and biological process, respectively. The results revealed that the elevated *LCN2* was significantly related to extracellular matrix organization and the protein digestion signaling pathway which had been widely reported to be related to the invasion of tumor cells (Figure S4B,C). The well-known extracellular matrix organization-related genes, matrix metalloproteinase (MMP) 2, 7, and 9, were verified to be increased in Daoy and ONS76 cells treated with recombinant *LCN2* [35] (Figure S4D). After treatment with si*LCN2*, the expression levels of MMP 2, 7, and 9 in Daoy and ONS76 were decreased (Figure S4E). These results indicate that *LCN2* secreted by TAAs in SHH-MB may promote the invasion of MB tumor cells through MMPs.

3.4 | The increased secretion of *LCN2* may be regulated by *STAT3* in TAAs of SHH-MB

LCN2 was reported as a *STAT3*-dependent upregulated factor in astrocyte [36]. Previous studies showed that *STAT3* is a key regulator of astrocyte reactivity associated with brain metastatic tumor [37–39]. To clarify whether the expression of *LCN2* was regulated by *STAT3* in TAAs of MB, we further detected the activation of *STAT3* in TAAs. The results showed that the expression of *LCN2*, *JAK2*, and the phosphorylation of *STAT3* (p-*STAT3*) at both tyrosine 705 and serine 727 were significantly increased in TAAs (Figure 4A–D, Figure S5A). Moreover, as upstream

FIGURE 3 *LCN2* was up-regulated in tumor-associated astrocytes and associated with the poor overall survival of MB. (A) Volcano plot displayed the differential expression genes between TAAs and the normal ASs. The red triangles and the green triangles represent differentially expressed up-regulated genes and down-regulated genes, respectively ($|\log_2FC| \geq 1.5, p \leq 0.05$). (B) Hierarchical clustering heat map of the differentially expressed genes between ASs and TAAs ($|\log_2FC| \geq 2$, false discovery rate ≤ 0.05). (C) Genes with significant differential expression levels in TAAs were verified by qPCR. (D) Flowchart of data analysis to search for the overall survival (OS)-correlated genes in TAAs. Among the total 757 upregulated and 407 downregulated genes identified in TAAs (shown in A), the prognostic significance of the most significant differentially expressed genes (shown in B) was evaluated by univariate Cox regression analysis of overall survival in patients with MB. Two positive-correlated genes (95% CI > 1) and one negative-correlated gene (95% CI < 1) associated with OS were finally selected. (E) Forest plot of the genes associated with OS of MB (statistical significance at the $p \leq 0.05$ level was considered as the potential prognostic factors). Kaplan–Meier curve showed the survival of MB patients with different expression level of *LCN2*: (F) total patients of four MB subgroups ($n = 374$), (G) patients with SHH-MB ($n = 105$) (HR, hazard ratio; CI, confidence interval). (H) The concentration of secreted protein *LCN2* in ASs co-cultured with Daoy or ONS-76 was quantified by ELISA. (I) Immunofluorescence staining was performed to detect the expression of *LCN2*, GFAP, and SYN in the MB tumor of mice model. The white arrows showed the co-localization of *LCN2* and GFAP. (J, K) The numbers of *LCN2*⁺*SYN*⁺ and *LCN2*⁺*GFAP*⁺ cells were counted with Photoshop software and normalized to the total number of total *LCN2*⁺ cells in each field ($n = 5$; five views were randomly captured for each tumor).

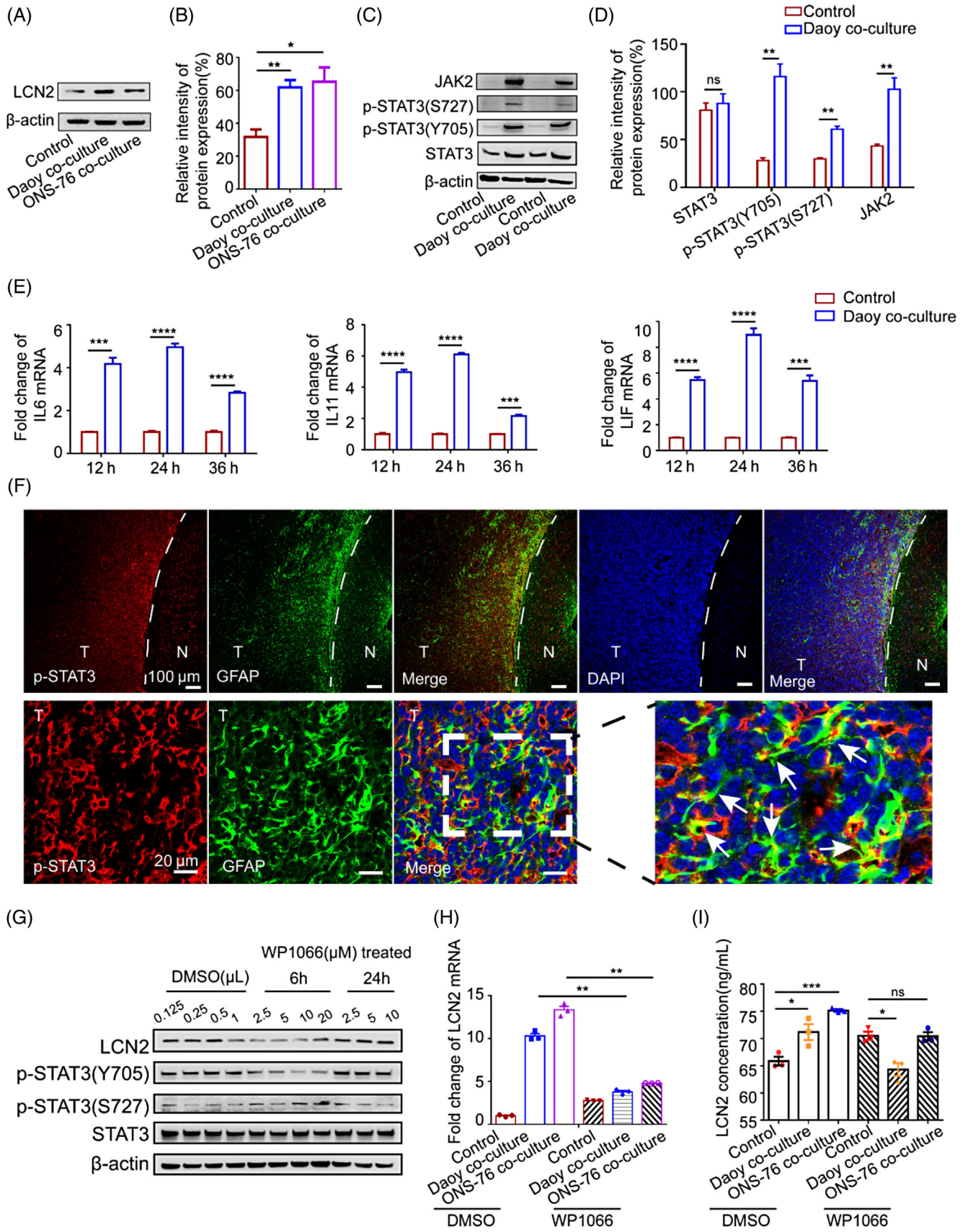


FIGURE 4 Legend on next page.

regulators of STAT3, the expression of IL6, IL11, and LIF significantly increased in TAAs (Figure 4E). All these results indicated that MB cells activated the JAK2/STAT3 pathway in TAAs.

Previous studies reported that SHH-MB tumor cells maintain stemness via the activation of JAK2/STAT3-mediated Notch signaling pathway by TAAs [12]. To explore whether the STAT3 was activated in SHH-MB tumor cells, we further detected the STAT3 pathway in MB cells within co-culture system. No significant change was observed for the phosphorylated STAT3 at both tyrosine 705 and serine 727 sites in Daoy co-cultured either with TAAs or with RAW264.7 (a mouse cell line of macrophage) (Figure S5B,C). These results indicated that the activation of STAT3 pathway mainly occurred in TAAs rather than tumor cells, which was confirmed by the transgenic mouse model. We found that the phosphorylated STAT3 (p-STAT3 [Y705]) mainly expressed in GFAP⁺ TAAs rather than the tumor cells of ND2-SmoA1 mice (Figure 4F). These results indicated that the STAT3 signaling pathway was mainly activated in TAAs rather than tumor cells in SHH-MB.

To further verify the LCN2 was upregulated by STAT3 in TAAs, we employed WP1066, a specific small-molecule inhibitor of STAT3, to treat ASs at different concentrations for 6 and 24 h, respectively. We found that, compared with the control group, 6 h treatment of WP1066 with concentrations of 2.5, 5, and 10 μ M significantly reduced the protein level of p-STAT3 (Y705) in ASs. After the inhibition of STAT3, the expression of LCN2 decreased. However, the expression of p-STAT3 (Y705) and LCN2 in ASs showed no significant change when the WP1066 treatment was prolonged to 24 h with the same concentrations (Figure 4G). Q-PCR and ELISA assay verified the above results (Figure 4H,I). Our data illustrated that the increased expression of LCN2 in the TAAs was correlated with the activation of JAK2/STAT3 pathway, which could be inhibited by STAT3 inhibitor.

3.5 | LCN2 knocked down in TAAs inhibited cell proliferation and migration ability of MB cells

To illustrate whether TAAs promote MB growth mainly through LCN2, we inhibited the expression of LCN2 in

TAAs either by STAT3 inhibitor (WP1066) or by synthetic small interfering RNAs (siRNAs) (Figure 5A). Using western blot analysis, we observed that the high expression of p-STAT3 (Y705) and LCN2 in TAAs could be effectively inhibited by WP1066 treatment with 1 and 2.5 μ M, respectively, at 24 h time point of co-culture (Figure 5B). After treatment by conditioned medium, the proliferation and migration ability of Daoy and ONS-76 were significantly inhibited by WP1066 (Figure 5C–E), implying that the effect of TAAs in tumor promotion could be restrained by down-regulating the expression of LCN2 via WP1066.

In order to exclude the possible effect of other cytokines and growth factors that are regulated by STAT3 in TAAs, TAAs were transiently transfected by siLCN2-1-3, respectively (Figure 5F–I). The siLCN2-3 which resulted in the most significant loss of LCN2 expression on both protein (~70%) and mRNA (~90%) levels was used in all subsequent experiments.

To further verify TAAs could promote tumor progression by LCN2, we performed parallel experiments by treating Daoy and ONS-76 with the conditioned medium of TAAs transfected with siLCN2-3 and siNC. The results showed that the siLCN2-3 transfection in TAAs significantly reduced the effect of TAAs on promoting the proliferation and migration ability of tumor cells (Figure 5J–L). We demonstrated that LCN2 expression in TAAs could significantly induce tumor progression in vitro.

3.6 | Inhibition of LCN2 could reduce tumor progression and prolong the survival time of the ND2SmoA1 MB mice

To further confirm the role of LCN2 in MB progression, we continued to explore whether the inhibition of LCN2 in TAAs affects the tumor growth in vivo. As a small molecule inhibitor of STAT3, WP1066 can cross the blood–brain barrier (BBB) [40]. MB mice bearing different volumes of tumors were randomly divided into two groups. WP1066 was injected intraperitoneally three times a week for 6 weeks. The tumor growth of MB mice were monitored during the treatment (Figure 6A).

The tumors of ND2-SmoA1 mice were shown at Day 0, 2 weeks, 4 weeks, and 6 weeks (Figure 6B). Tumor

FIGURE 4 LCN2 may be modulated by STAT3 in the tumor-associated astrocytes. (A) The expression of LCN2 protein in TAAs was detected by western blot. (B) The expression of LCN2 was quantified by Image J. (C) The protein expression of JAK2, STAT3, phosphorylated STAT3 at tyrosine 705 and serine 727 (p-STAT3 Y705, p-STAT3 S727) was detected by western blot in TAAs. (D) The expression of STAT3, p-STAT3 (Y705), p-STAT3 (S727), and JAK2 was quantified by Image J. (E) The RNA expression of IL6, IL11, and LIF in TAAs was detected by q-PCR. (F) Immunofluorescence staining of p-stat3 (Y705) and GFAP in ND2SmoA1 MB mice. The white arrows indicated the co-localization of p-STAT3 with GFAP. (G) ASs were treated with different concentration of WP1066 (STAT3 inhibitor) for 6 and 24 h. The control group was treated with corresponding volume of DMSO. Cell lysates were harvested and the protein expression of STAT3, p-STAT3 (Y705), p-STAT3 (S727), and LCN2 was detected by western blot. TAAs were treated with WP1066 at the concentration of 10 μ M for 6 h, the cells were harvested and the expression of LCN2 was detected in TAAs by q-PCR (H) and ELISA (I). Images are representative, and values are expressed as the mean \pm SEM from at least three independent experiments. *p*-values are determined by *t* test (D, E) or one-way ANOVA (H, I).

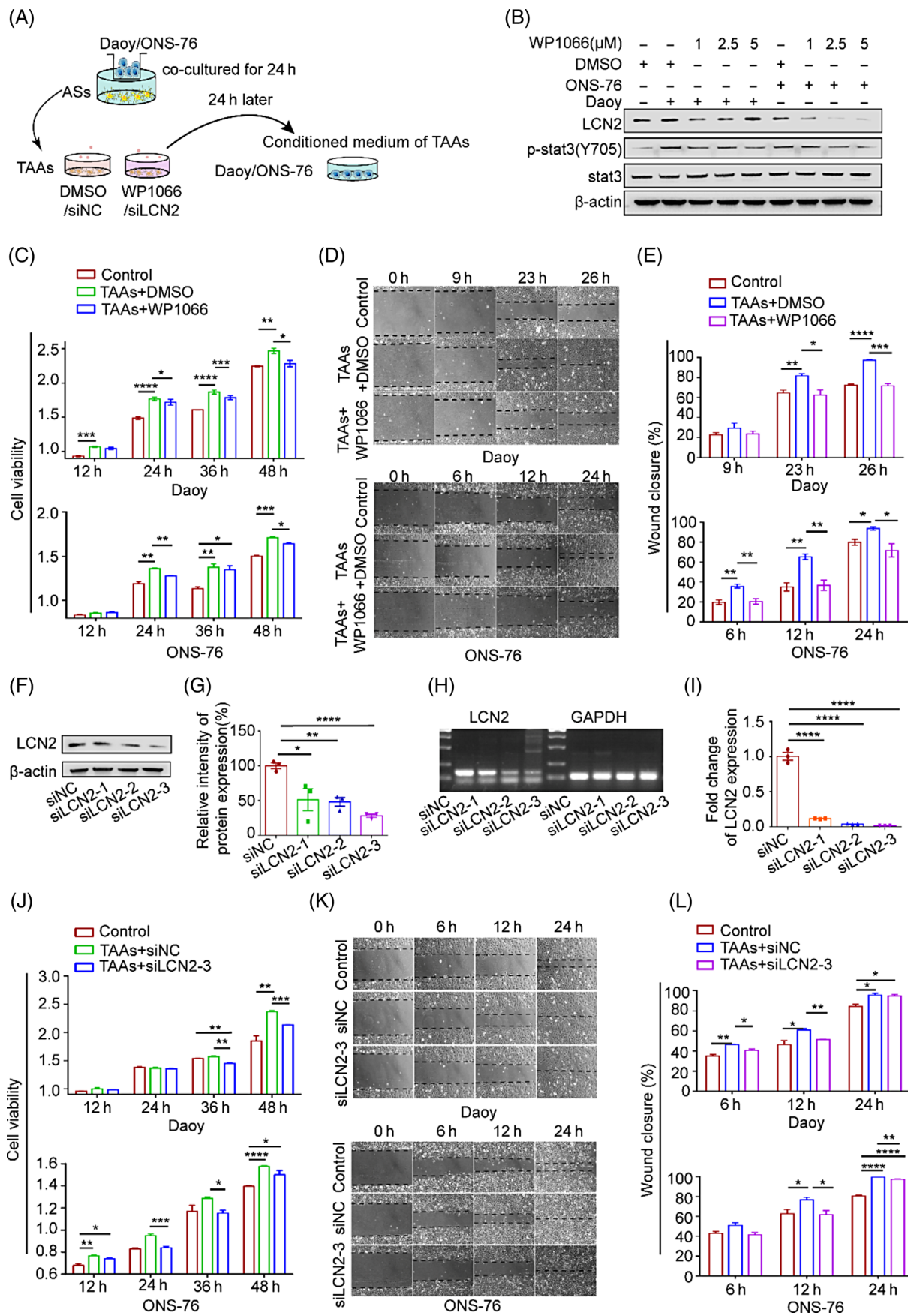


FIGURE 5 Legend on next page.

growth analysis showed that WP1066 significantly retarded the MB growth. Tumor volume significantly decreased after 3 weeks of drug treatment (Figure 6C). Kaplan–Meier survival analysis showed that the OS of MB mice was significantly improved after the treatment (Figure 6D), indicating that WP1066 retarded the tumor progression in ND2SmoA1 mice.

To validate whether WP1066 inhibits STAT3 in the tumor tissue, we examined the protein expression of p-STAT3 in the tumor-bearing MB mice treated by WP1066 or vehicle. We found that the p-STAT3 expression was significantly decreased in the tumors of mice with WP1066 treatment compared with the vehicle group (Figure S6A,B), indicating that the effects of WP1066 inhibiting STAT3 were on the target. To investigate whether the inhibitory effect of WP1066 in MB mice was achieved by down-regulating the expression of LCN2 in TAAs, we collected brain tissue of the mice and analyzed the expression of LCN2 by immunofluorescence. We found that WP1066 treatment reduced the expression of LCN2 in TAAs significantly (Figure 6E,F). More importantly, although no significant change was observed in the distribution pattern of TAAs, the proliferation ability of tumor cells at the tumor margin was significantly reduced in mice after WP1066 treatment. However, no significant difference in tumor proliferation ability was observed at the tumor center (Figure 6G,H), which seems that the inhibition effect on tumor growth by WP1066 was related to the TAAs in MB. Our results in vivo showed that WP1066 could reduce the expression of LCN2 in TAAs by inhibiting the activation of STAT3 and finally inhibit the MB progression.

3.7 | AAV-sh-*Lcn2* efficiently improved the antitumor activity of SMO inhibitor in ND2SmoA1 MB mice

To further investigate the inhibitory effect of targeting LCN2 for MB treatment, we selectively knocked down LCN2 in astrocytes by AAV delivery of sh-*Lcn2* carried with astrocyte-specific promoter in ND2-SmoA1 MB mice (Figure 7A). The AAV serotype of PHP.eB which

has been reported to cross the BBB effectively was used to avoid the interventional intracerebral injection [41]. MB mice bearing various volumes of tumors were randomly divided into four groups. AAV-sh-*Lcn2* or AAV-scramble was administered intravenously at Day 0. Smo inhibitor (Sonidegib) or vehicle with the same dose (20 mg/kg) was given daily during the experiments. MRI was used routinely to monitor the tumor growth in vivo (Figure 7B).

In order to detect whether the AAV vectors infect the astrocytes specifically, the astrocyte-specific expression of eGFP was confirmed by immunofluorescence staining in mice 4 weeks after AAV injection (Figure 7C). To further assess the knockdown efficiency of sh-*Lcn2* in TAAs in vivo, we collected brain tissues of the mice and analyzed the expression of LCN2 in tumor by immunofluorescence. The results showed that the expression of LCN2 in eGFP⁺ TAAs was reduced significantly in AAV-sh-*Lcn2*-injected mice compared with controls ($p < 0.0001$) (Figure 7D,E). These results revealed that the AAV sh-*Lcn2* vector could specifically knock down the expression of LCN2 in TAAs in vivo.

To further explore the antitumor efficiency of AAV-sh-*Lcn2* alone or its combination with Sonidegib, we measured the tumor size every 10 days in parallel groups. The tumors of ND2-SmoA1 mice in the four groups were shown at Day 0, 20, 40, and 60 (Figure 7F). Survival analysis showed that compared to the control group (AAV-scramble + Vehicle), either AAV-sh-*Lcn2* (AAV-sh-*Lcn2* + Vehicle, $p = 0.0332$) or Sonidegib (AAV-scramble + Sonidegib, $p = 0.0043$) alone, and the combination therapy (AAV-sh-*Lcn2* + Sonidegib, $p = 0.0088$) were all able to significantly prolong the survival time of SHH-MB mice (Figure 7G). The tumor growth of mice was significantly retarded when treated with AAV-sh-*Lcn2* or/and Sonidegib compared to the control group 20 days after treatment. Moreover, AAV-sh-*Lcn2* efficiently reduced the drug resistance and improved the antitumor activity of SMO inhibitor in ND2-SmoA1 MB mice significantly ($p = 0.0423$) (Figure 7H). Overall, these results showed that anti-tumor efficacy was enhanced using combination therapy compared to classical targeted treatment alone. Therefore, we were convinced that LCN2

FIGURE 5 LCN2 knocked down in TAAs inhibited cell proliferation and migration ability of MB tumor cells. (A) Illustration of workflow: in order to inhibit the expression of LCN2, TAAs were treated with WP1066 or siRNA for 24 h, the corresponding conditioned medium (TAAs + DMSO, TAAs + WP1066, TAAs + siNC, and TAAs + siLCN2) were obtained. The proliferation and migration of MB tumor cells were assessed, and the control group was treated with the normal culture medium. (B) TAAs were treated by different concentrations (1, 2.5, and 5 μ M) of WP1066 for 24 h. Control groups were treated by the corresponding volume of DMSO. The expression of STAT3, p-STAT3 (Y705), and LCN2 in TAAs was detected by western blot. CCK8 (C) and wound healing (D) assay were performed for the proliferation and migration analysis of Daoy and ONS-76 treated with conditioned medium of TAAs + DMSO, TAAs + WP1066, and the control medium. (E) Wound healing areas of Daoy and ONS-76 at different time points were quantified by imageJ. (F) Western blot was used to detect the protein level of LCN2 in TAAs transfected with siNC or siLCN2. (G) Quantitative relative intensity analysis of western blot for the expression of LCN2 in TAAs by Image J. (H) RT-PCR was performed to verify the knockdown efficiency of LCN2-siRNA in TAAs. (I) The mRNA levels of LCN2 in TAAs transfected with siNC and siLCN2 were assessed by q-PCR. CCK8 assay (J) and wound healing assay (K) were performed to analyze the proliferation and migration ability of Daoy and ONS-76 treated with the conditioned medium of TAAs + siNC, TAAs + siLCN2-3. (L) Wound healing areas of Daoy and ONS-76 at different time points were quantified by imageJ. The percentage of wound closure at each time point was normalized based on the wound area of 0 h. Images are representative, and values are expressed as the mean \pm SEM from at least three independent experiments. p -values are determined by t test.

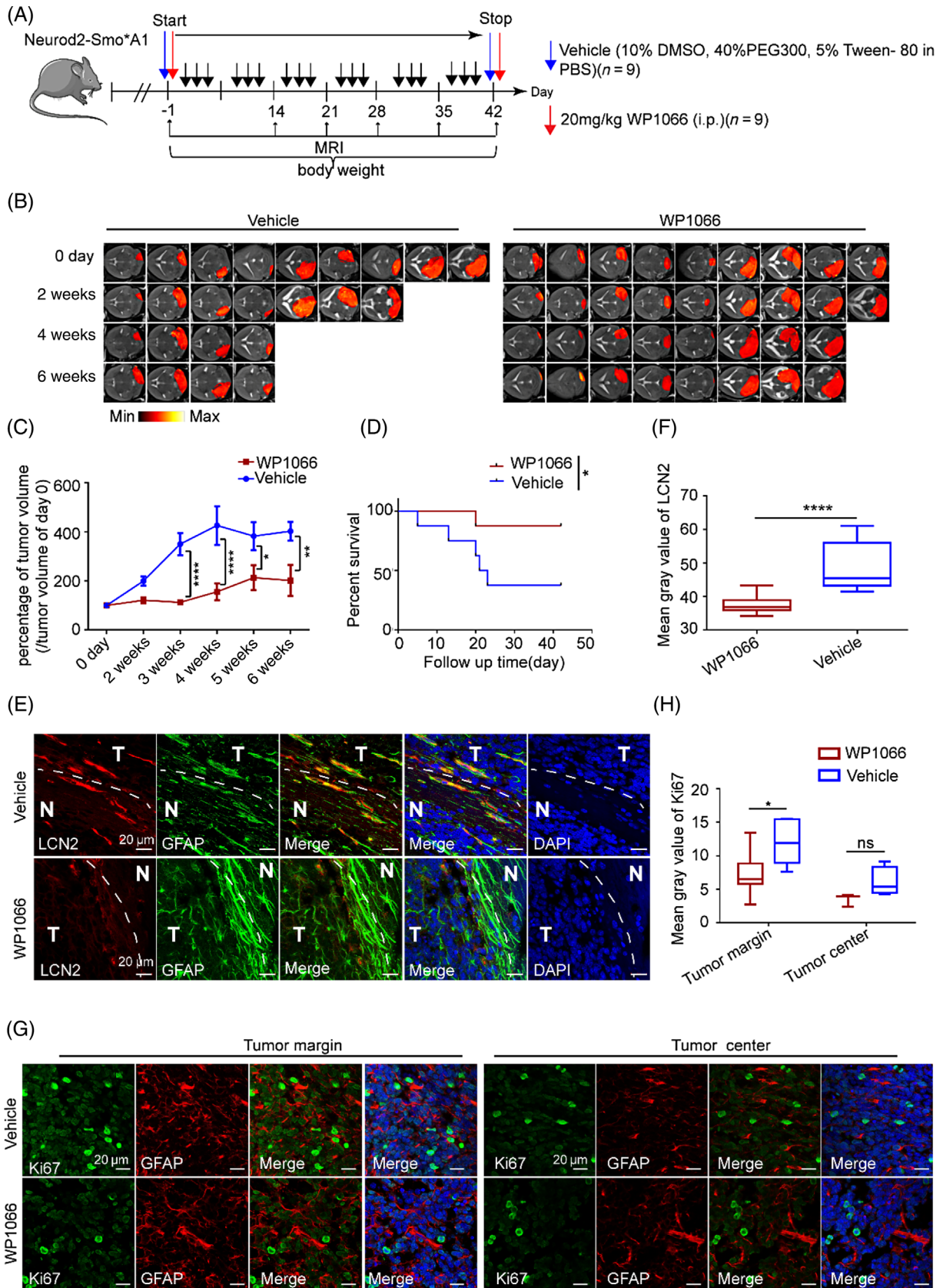


FIGURE 6 Legend on next page.

would be a potential and promising drug target of SHH-MB.

4 | DISCUSSION

Astrocytes are of increasing interest for their pivotal role in normal brain development and pathological processes in central nervous system including neurodegenerative diseases and brain tumors [11, 16, 37, 38, 42]. Astrocytes in the TME called TAAs show the immune characteristics with enhanced reactivity and have a close relationship with tumor dissemination and metastasis [43]. However, until now, few studies have clarified the dynamic changes of TAAs during the MB progression. In the present study, we show the distribution characteristics of TAAs at different time points during tumor growth in the transgenic SHH-MB mouse model. It is our novel finding that increased expression of LCN2 in TAAs was closely correlated with the MB progression.

Our previous study reported that the M2 macrophages in TME of MB increased with the age of SHH-MB-bearing mice [10]. Here, we observed different distribution patterns of the TAAs during tumor growth. TAAs, which were evenly distributed in SG tumors, gathered to the margin of the LG tumors, forming “glia scar.” Glial scar is the result of the increased reactivity and proliferation of astrocytes in the brain after injury. The activated astrocytes will eventually lead to dysfunction, overexcitation, or death of neurons [44, 45]. In our study, the heterogeneity of TAAs in MB led to the difference in proliferation and migration abilities between tumor cells in the margin and those in the center. Considering the effect of TAAs on the biological functions of tumor cells, we speculated that MB cells would eventually reprogram the adapted microenvironment by “instigating” a tumor-promoting phenotype of TAAs.

In the present study, the specific distribution of TAAs leads to a heterogeneous proliferative ability of tumor cells at different tumor stages. This is consistent with previous study that the number of TAAs in the relapsed MB is significantly higher than that of primary tumors [11]. Recent study reported that tumor-associated macrophages (TAMs) including microglia and monocyte-derived macrophages display different dimensions during different

stages of SHH-MB in mouse model [9]. Here, we found that the reactivity and distribution pattern of TAAs in MB were also related to the tumor stage. At the early stage, they were evenly distributed within the tumor. Redistribution occurred during tumor growth. TAAs gathered at the tumor margin, resulting in the higher proliferative ability of tumor cells there than tumor cells in the center (Figure 1B, Figure S1A). However, the regulating mechanism about the process still remains unclear. The increased TAAs in different tumor stages of SHH-MB may include proliferative astrocytes, normal astrocytes attracted to the tumor mass and trans-differentiated astrocytes [9, 11, 46]. In our SHH-MB mouse model, the TAAs we detected were less proliferative than tumor cells. Whether the TAAs come from normal reactive astrocytes, or the tumor-derived astrocytes during MB progression remains to be determined.

LCN2 is a member of lipocalin family. It was first identified in the urine of mice with SV40-infected kidneys [47]. Up-regulation of LCN2 in tumor cells, such as breast cancer, colorectal cancer, and pancreatic cancer was reported to be related to tumor progression and therapeutic resistance [48–50]. The cellular origin of LCN2 in the brain and its role in different diseases were unclear [19, 23, 51–53]. In the present study, we clarified that high expression of LCN2 in TAAs was closely related with the increased proliferation and migration ability of SHH-MB both in vitro and in vivo. This result is consistent with the previous study which reported that there was statistical correlation between LCN2 and high histological grade of glioblastoma [54]. Besides SHH-MB, we also found the increased expression of LCN2 was correlated with the poor survival of G3-, G4-MB patients (Figure S3B–D). This result indicated that LCN2 may be a promising candidate target in SHH-, G3-, and G4-MB combination therapy. More studies on the functions of LCN2 in G3-, and G4-MB are remained to be explored.

As an inflammatory molecule, LCN2 is regulated by a variety of cytokines and transcription factors, such as IL-10, NF κ B, and STATs [49, 52]. The increased expression of LCN2 in endothelial cells was considered to be related to the activation of STAT3/LCN2 signal pathway by exosomes derived from glioblastoma [23]. JAK/STAT3 pathway also plays a key regulatory role in the signal cascade related to astrocyte reactivity [55]. It was

FIGURE 6 Inhibition of LCN2 retarded the tumor progression of MB in the ND2SmoA1 MB mice model. (A) Schematic illustration of the experimental design. Mice were randomly divided and treated with DMSO (Vehicle group) or WP1066 (WP1066-treated group), and the tumorigenesis of mice were monitored by MRI. (B) Representative MRI images of each mouse at 2, 4, or 6 weeks ($n = 9$ in each group). (C) Tumor volumes of mice during administration. Tumor volume on Day 0 was set as 100, tumor volume at each time point was shown after normalization. (D) Kaplan–Meier survival analysis was performed to identify the survival of mice. (E) Immunofluorescence staining of GFAP in green color and LCN2 in red color was performed to determine the expression of LCN2 in TAAs of MB mice treated with WP1066 and Vehicle. (F) The mean immunofluorescence pixel intensity of LCN2 was quantified by ImageJ software. (G) The distribution pattern of astrocytes and the proliferation ability of tumor cells in tumor margin (left) and tumor center (right) were determined in both vehicle (up) and WP1066-treated (down) group of MB mice by GFAP (red color) and Ki67 (green color) immunofluorescence staining, respectively. (H) The mean immunofluorescence pixel intensity of Ki67 was quantified by ImageJ software (three pictures were randomly captured for each tumor, $n = 4$). p -values are determined by two-way ANOVA (C, H), t test (F), or log-rank (Mantel–Cox) test. Images are representative, and values are expressed as the mean \pm SEM.

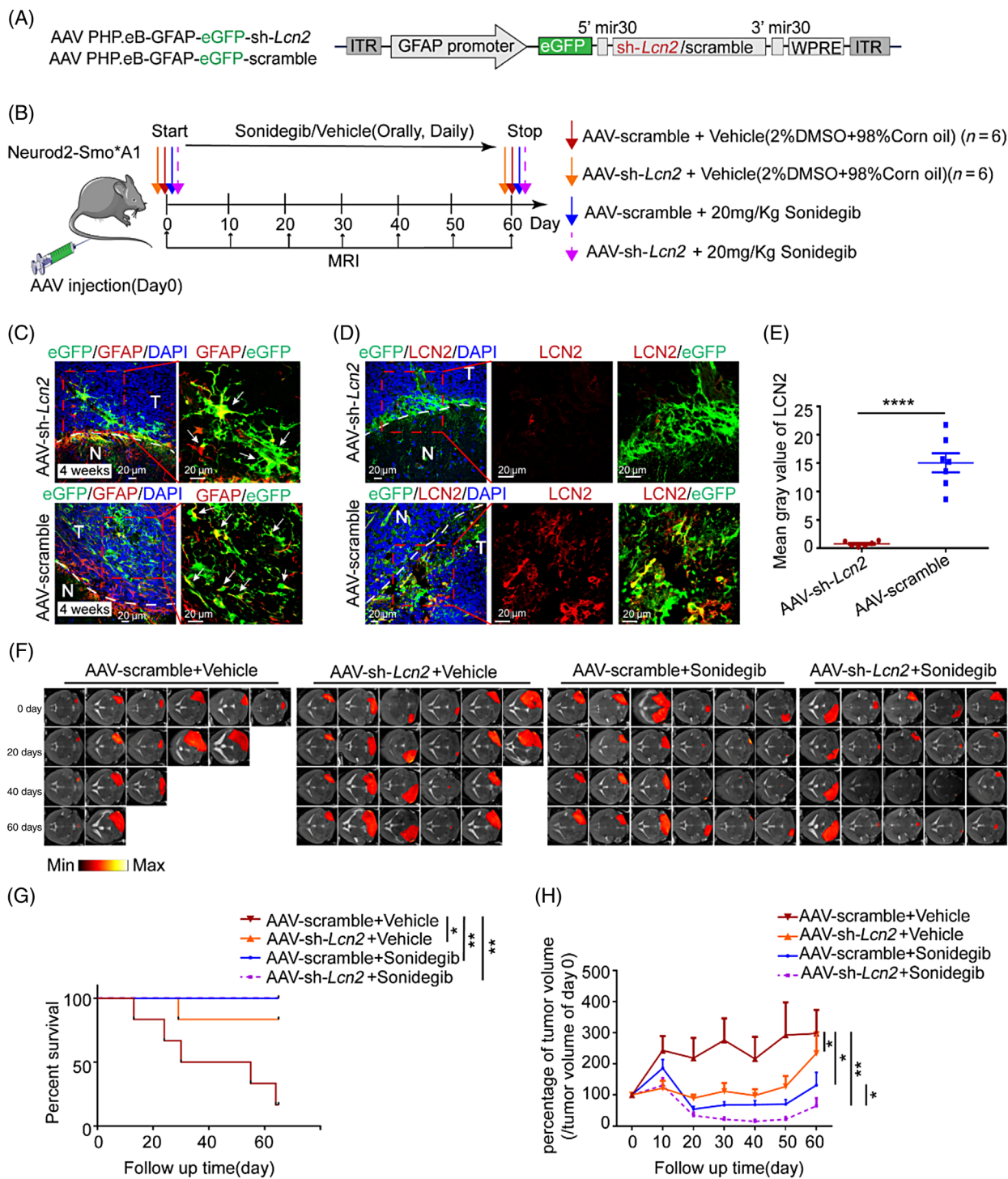


FIGURE 7 Specific knockdown of LCN2 in astrocytes improved the antitumor activity of Sonidegib in ND2SmoA1 MB mice. (A) Schematic of the elementary components AAV-shRNA vector used in this study. (B) Schematic illustration of a schedule for AAV injection and Sonidegib treatment. Mice were injected with AAV-shLcn2 or AAV-scramble via tail vein at Day 0. Sonidegib and Vehicle were orally administrated every day, and the tumorigenesis of mice was monitored by MRI (six mice for AAV-scramble + Vehicle, six for AAV-scramble + Sonidegib, six for AAV-shLcn2 + Vehicle, and five for AAV-shLcn2 + Sonidegib). (C) Immunofluorescence staining of astrocytes with GFAP in red color. Confocal images of the astrocyte-specific expression of eGFP 4 weeks after the AVV injection. (D) Immunofluorescence staining of LCN2 in red color was performed to determine the expression of LCN2 in eGFP+ TAA of MB mice injected with AAV-shLcn2 and AAV-scramble. (E) The mean immunofluorescence pixel intensity of LCN2 was quantified by ImageJ software (Photos were taken using the same exposure and magnification settings, five pictures were randomly captured for the tumor of each mouse, $n = 7$). (F) Representative MRI images of each mouse at 0, 10, 40, and 60 days. (G) Kaplan-Meier survival analysis was performed to identify the survival of mice. (H) Tumor volumes of mice during administration. Tumor volume on Day 0 was set as 100, tumor volume at each time point was shown after normalization, and the statistical marker in the figure was the statistical difference among each group at the time point of 50 days. p -values are determined by t test (E, H), log-rank (Mantel-Cox) test (G), and values are expressed as the mean \pm SEM.

reported that the up-regulation of p-STAT3 in astrocytes promoted the tumor progression of various metastatic malignancies [37]. Our current study showed that inhibiting the activation of JAK2/STAT3 in TAAs by STAT3 inhibitor (WP1066) could inhibit the proliferation of SHH-MB both in vitro and in vivo. WP1066 could significantly inhibit the expression of LCN2 in TAAs and had great potential advantages in the treatment of MB. It is worth noting that the effective time of WP1066 on STAT3 and LCN2 was limited, as shown in Figures 4G and 5B. This may be related with the inhibitory effect of WP1066 on STAT3 can lead to expression alterations of other molecules in the same pathway, such as JAK2 and ERK1/2, which has been confirmed by other studies of WP1066 in vitro [56]. Moreover, as WP1066 is not a specific inhibitor for TAAs, its clinical safety and effectiveness need to be further evaluated. Compared with the wide expression of STAT3, LCN2 is specifically expressed in the brain under pathological conditions. Notably, our results have shown that anti-tumor efficacy of knocking down LCN2 combined with Sonidegib treatment was enhanced compared to Sonidegib treatment alone in the ND2SmoA1 MB mice model, indicating that combined targeted therapy strategy improved the effect of classical targeted therapy of MB. Hence, LCN2 is expected to become a novel and promising therapeutic target for MB patients, especially for SHH-MB.

In conclusion, we elucidated the key regulatory mechanism of TAAs during MB progression. We first clarified that LCN2 in MB was correlated to the poor prognosis of MB patients. LCN2 in MB was mainly secreted from TAAs, which was regulated by the JAK2/STAT3 pathway. Through the drug intervention experiment in the SHH-MB mouse model, we preliminarily discussed the feasibility of LCN2 as a potential molecular target of MB.

AUTHOR CONTRIBUTIONS

Haishuang Li, Yuqing Liu, and Qing Chang performed experiments, analyzed data, and wrote the manuscript. Luzheng Xu contributed to MRI analysis. Yuqing Liu and Ziwen Sun assisted with the maintenance of mice and animal euthanasia. Xiaodan Liu, Hui Liang, Chen Song, and Yu Zhang developed the idea for the study. Danfeng Zheng and Bao Yang involved in pathologic diagnosis and analysis. Qing Chang, Jianyuan Luo, and Xiaodan Liu conceived the study and oversaw overall direction and planning. All authors discussed the results and commented on the manuscript. Qing Chang was responsible for the overall supervision of the project and data analysis.

ACKNOWLEDGMENTS

This study was supported by the National Natural Science Foundation of China (Nos. 81972353, 81101900, and 30540008), the Beijing Natural Science Foundation (Nos. 7192095 and 7232098), Beijing Health Commission

Foundation (11000023T000002044300-4), and the Beijing Key Laboratory of Research and Transformation of Biomarkers for Neurodegenerative Diseases, Peking University Third Hospital (No. BZ0436). We appreciate Xiu Wu Bian's Lab for providing cell line.

CONFLICT OF INTEREST STATEMENT

All authors have no conflict of interest regarding the publication of this article.

DATA AVAILABILITY STATEMENT

For patient data analysis, the expression profiling of 374 primary medulloblastoma samples which were subtyped into 105 SHH, 38 WNT, 76 Group 3, and 156 Group 4 were used under the accession number GSE85218. All the clinical data of the primary medulloblastoma cohort are available via supplementary table 1 of the paper entitled "Intertumoral Heterogeneity within Medulloblastoma Subgroups" (<https://www.sciencedirect.com/science/article/pii/S1535610817302015?via%3Dihub>). Raw microarray sequencing data are also available for this dataset via the Gene Expression Omnibus (GEO) accession numbers GSE85218 and GSE54962; however, the publicly available normalized matrix was used. Information about all other data and reagents described under results will be made freely available from the corresponding author Qing Chang on request.

ORCID

Haishuang Li  <https://orcid.org/0009-0004-9023-7059>

Yuqing Liu  <https://orcid.org/0000-0002-5119-2984>

Qing Chang  <https://orcid.org/0000-0001-5138-8760>

REFERENCES

- Fang FY, Rosenblum JS, Ho WS, Heiss JD. New developments in the pathogenesis, therapeutic targeting, and treatment of pediatric medulloblastoma. *Cancers (Basel)*. 2022;14(9):2285.
- Cotter JA, Hawkins C. Medulloblastoma: WHO 2021 and beyond. *Pediatr Dev Pathol*. 2022;25(1):23–33.
- Perreault S, Ramaswamy V, Achrol AS, Chao K, Liu TT, Shih D, et al. MRI surrogates for molecular subgroups of medulloblastoma. *Am J Neuroradiol*. 2014;35(7):1263–9.
- Waszak SM, Robinson GW, Gudenbas BL, Smith KS, Forget A, Kojic M, et al. Germline elongator mutations in Sonic Hedgehog medulloblastoma. *Nature*. 2020;580(7803):396–401.
- Yan H, Zabih V, Bartels U, Das S, Nathan P, Gupta S. Prognostic factors related to overall survival in adolescent and young adults with medulloblastoma: a systematic review. *Neurooncol Adv*. 2022;4(1):vdac016.
- Martin AM, Raabe E, Eberhart C, Cohen KJ. Management of pediatric and adult patients with medulloblastoma. *Curr Treat Options Oncol*. 2014;15(4):581–94.
- Yock TI, Yeap BY, Ebb DH, Weyman E, Eaton BR, Sherry NA, et al. Long-term toxic effects of proton radiotherapy for paediatric medulloblastoma: a phase 2 single-arm study. *Lancet Oncol*. 2016;17(3):287–98.
- de Pablos-Aragoneses A, Valiente M. An inbred ecosystem that supports medulloblastoma. *Immunity*. 2020;52(3):431–3.
- Yao M, Ventura PB, Jiang Y, Rodriguez FJ, Wang L, Perry JSA, et al. Astrocytic trans-differentiation completes a multicellular

- paracrine feedback loop required for medulloblastoma tumor growth. *Cell*. 2020;180(3):502–520.e19.
10. Zhu L, Yang Y, Li H, Xu L, You H, Liu Y, et al. Exosomal microRNAs induce tumor-associated macrophages via PPAR-gamma during tumor progression in SHH medulloblastoma. *Cancer Lett*. 2022;535:215630.
 11. Guo D, Wang Y, Cheng Y, Liao S, Hu J, Du F, et al. Tumor cells generate astrocyte-like cells that contribute to SHH-driven medulloblastoma relapse. *J Exp Med*. 2021;218(9):e20202350.
 12. Liu HL, Sun YL, Franco-Barraza J, Wang ZJ, Yu XG, Feng SY. Necroptotic astrocytes contribute to maintaining stemness of disseminated medulloblastoma through Ccl2 secretion. *Neuro Oncol*. 2020;22:202–3.
 13. Gong B, Guo D, Zheng C, Ma Z, Zhang J, Qu Y, et al. Complement C3a activates astrocytes to promote medulloblastoma progression through TNF-alpha. *J Neuroinflammation*. 2022;19(1):159.
 14. Sofroniew MV, Vinters HV. Astrocytes: biology and pathology. *Acta Neuropathol*. 2010;119(1):7–35.
 15. Rickert CH, Paulus W. Prognosis-related histomorphological and immunohistochemical markers in central nervous system tumors of childhood and adolescence. *Acta Neuropathol*. 2005;109(1):69–92.
 16. Liu H, Sun Y, O'Brien JA, Franco-Barraza J, Qi X, Yuan H, et al. Necroptotic astrocytes contribute to maintaining stemness of disseminated medulloblastoma through CCL2 secretion. *Neuro Oncol*. 2020;22(5):625–38.
 17. Flower DR, North AC, Sansom CE. The lipocalin protein family: structural and sequence overview. *Biochim Biophys Acta*. 2000;1482(1–2):9–24.
 18. Cowland JB, Borregaard N. Molecular characterization and pattern of tissue expression of the gene for neutrophil gelatinase-associated lipocalin from humans. *Genomics*. 1997;45(1):17–23.
 19. Jha MK, Lee S, Park DH, Kook H, Park KG, Lee IK, et al. Diverse functional roles of lipocalin-2 in the central nervous system. *Neurosci Biobehav Res*. 2015;49:135–56.
 20. Marques F, Mesquita SD, Sousa JC, Coppola G, Gao FY, Geschwind DH, et al. Lipocalin 2 is present in the EAE brain and is modulated by natalizumab. *Front Cell Neurosci*. 2012;6:33.
 21. Liu MF, Jin T, Shen JH, Shen ZY, Zheng ZC, Zhang ZL, et al. NGAL and NGALR are frequently overexpressed in human gliomas and are associated with clinical prognosis. *J Neurooncol*. 2011;104(1):119–27.
 22. Zheng LT, Lee S, Yin GN, Mori K, Suk K. Down-regulation of lipocalin 2 contributes to chemoresistance in glioblastoma cells. *J Neurochem*. 2009;111(5):1238–51.
 23. Yang C, Wu Y, Wang L, Li SD, Zhou JH, Tan YL, et al. Glioma-derived exosomes hijack the blood-brain barrier to facilitate nanocapsule delivery via LCN2. *J Control Release*. 2022;345:537–48.
 24. Velasco-Estevéz M, Rolle SO, Mampay M, Dev KK, Sheridan GK. Piezo1 regulates calcium oscillations and cytokine release from astrocytes. *Glia*. 2020;68(1):145–60.
 25. Maximov V, Chen Z, Wei Y, Robinson MH, Herting CJ, Shanmugam NS, et al. Tumour-associated macrophages exhibit anti-tumoural properties in Sonic Hedgehog medulloblastoma. *Nat Commun*. 2019;10(1):2410.
 26. Xiang X, Tang X, Yu Y, Xie S, Liu L, Chen M, et al. Role of lipocalin-2 in surgery-induced cognitive decline in mice: a signal from neuron to microglia. *J Neuroinflammation*. 2022;19(1):92.
 27. Justus CR, Leffler N, Ruiz-Echevarria M, Yang LV. In vitro cell migration and invasion assays. *J Vis Exp*. 2014;88:51046.
 28. Kim D, Langmead B, Salzberg SL. HISAT: a fast spliced aligner with low memory requirements. *Nat Methods*. 2015;12(4):357–60.
 29. Shen W, Song Z, Zhong X, Huang M, Shen D, Gao P, et al. Sangerbox: a comprehensive, interaction-friendly clinical bioinformatics analysis platform. *iMeta*. 2022;1(3):e36.
 30. Gronseth E, Gupta A, Koceja C, Kumar S, Kutty RG, Rarick K, et al. Astrocytes influence medulloblastoma phenotypes and CD133 surface expression. *PLoS One*. 2020;15(7):e0235852.
 31. Liu YQ, Yuelling LW, Wang Y, Du F, Gordon RE, O'Brien JA, et al. Astrocytes promote medulloblastoma progression through hedgehog secretion. *Cancer Res*. 2017;77(23):6692–703.
 32. Crescenzi E, Leonardi A, Pacifico F. NGAL as a potential target in tumor microenvironment. *Int J Mol Sci*. 2021;22(22):12333.
 33. Xu WX, Zhang J, Hua YT, Yang SJ, Wang DD, Tang JH. An integrative pan-cancer analysis revealing LCN2 as an oncogenic immune protein in tumor microenvironment. *Front Oncol*. 2020;10:605097.
 34. Holden VI, Lenio S, Kuick R, Ramakrishnan SK, Shah YM, Bachman MA. Bacterial siderophores that evade or overwhelm lipocalin 2 induce hypoxia inducible factor 1 alpha and proinflammatory cytokine secretion in cultured respiratory epithelial cells. *Infect Immun*. 2014;82(9):3826–36.
 35. Oh J, Takahashi R, Kondo S, Mizoguchi A, Adachi E, Sasahara RM, et al. The membrane-anchored MMP inhibitor RECK is a key regulator of extracellular matrix integrity and angiogenesis. *Cell*. 2001;107(6):789–800.
 36. Shiratori-Hayashi M, Koga K, Tozaki-Saitoh H, Kohro Y, Toyonaga H, Yamaguchi C, et al. STAT3-dependent reactive astrogliosis in the spinal dorsal horn underlies chronic itch. *Nat Med*. 2015;21(8):927–31.
 37. Priego N, Zhu L, Monteiro C, Mulders M, Wasilewski D, Bindeman W, et al. STAT3 labels a subpopulation of reactive astrocytes required for brain metastasis. *Nat Med*. 2018;24(7):1024–35.
 38. Shen MH, Kang YB. pSTAT3(+) reactive astrocytes promote brain metastasis. *Trends Mol Med*. 2018;24(9):733–5.
 39. Soto MS, Larkin JR, Martin C, Khrapitchev AA, Maczka M, Economopoulos V, et al. STAT3-mediated astrocyte reactivity associated with brain metastasis contributes to neurovascular dysfunction. *Cancer Res*. 2020;80(24):5642–55.
 40. Stechishin OD, Luchman HA, Ruan YB, Blough MD, Nguyen SA, Kelly JJ, et al. On-target JAK2/STAT3 inhibition slows disease progression in orthotopic xenografts of human glioblastoma brain tumor stem cells. *Neuro Oncol*. 2013;15(2):198–207.
 41. Dayton RD, Grames MS, Klein RL. More expansive gene transfer to the rat CNS: AAV PHP.EB vector dose-response and comparison to AAV PHP.B. *Gene Ther*. 2018;25(5):392–400.
 42. Sofroniew MV. Astrocyte reactivity: subtypes, states, and functions in CNS innate immunity. *Trends Immunol*. 2020;41(9):758–70.
 43. Katsetos CD, Del Valle L, Legido A, de Chadarevian JP, Perentes E, Mork SJ. On the neuronal/neuroblastic nature of medulloblastomas: a tribute to Pio del Rio Hortega and Moises Polak. *Acta Neuropathol*. 2003;105(1):1–13.
 44. Robel S, Buckingham SC, Boni JL, Campbell SL, Danbolt NC, Riedemann T, et al. Reactive astrogliosis causes the development of spontaneous seizures. *J Neurosci*. 2015;35(8):3330–45.
 45. Shandra O, Winemiller AR, Heithoff BP, Munoz-Ballester C, George KK, Benko MJ, et al. Repetitive diffuse mild traumatic brain injury causes an atypical astrocyte response and spontaneous recurrent seizures. *J Neurosci*. 2019;39(10):1944–63.
 46. Eberhart C. Astrocytes: new stars in the medulloblastoma firmament. *Neuro Oncol*. 2020;22(5):587–9.
 47. Hrabá-Renevey S, Turler H, Kress M, Salomon C, Weil R. SV40-induced expression of mouse gene 24p3 involves a post-transcriptional mechanism. *Oncogene*. 1989;4(5):601–8.
 48. Oren B, Urošević J, Mertens C, Mora J, Guiu M, Gomis RR, et al. Tumour stroma-derived lipocalin-2 promotes breast cancer metastasis. *J Pathol*. 2016;239(3):274–85.
 49. Rodvold JJ, Mahadevan NR, Zanetti M. Lipocalin 2 in cancer: when good immunity goes bad. *Cancer Lett*. 2012;316(2):132–8.

50. Santiago-Sanchez GS, Pita-Grisanti V, Quinones-Diaz B, Gumper K, Cruz-Monserrate Z, Vivas-Mejia PE. Biological functions and therapeutic potential of lipocalin 2 in cancer. *Int J Mol Sci.* 2020;21(12):4365.
51. Chia WJ, Dawe GS, Ong WY. Expression and localization of the iron-siderophore binding protein lipocalin 2 in the normal rat brain and after kainate-induced excitotoxicity. *Neurochem Int.* 2011;59(5):591–9.
52. Ferreira AC, Da Mesquita S, Sousa JC, Correia-Neves M, Sousa N, Palha JA, et al. From the periphery to the brain: Lipocalin-2, a friend or foe? *Prog Neurobiol.* 2015;131:120–36.
53. Naude PJW, Csaba N, Eiden LE, Ait-Ali D, van der Heide R, Engelborghs S, et al. Lipocalin 2: novel component of proinflammatory signaling in Alzheimer's disease. *FASEB J.* 2012;26(7):2811–23.
54. Barresi V, Tuccari G, Barresi G. NGAL immunohistochemical expression in brain primary and metastatic tumors. *Clin Neuro-pathol.* 2010;29(5):317–22.
55. Ceyzeriat K, Abjean L, Carrillo-de Sauvage MA, Ben Haim L, Escartin C. The complex states of astrocyte reactivity: how are they controlled by the Jak-Stat3 pathway? *Neuroscience.* 2016;330:205–18.
56. Judd LM, Menheniott TR, Ling H, Jackson CB, Howlett M, Kalantzis A, et al. Inhibition of the JAK2/STAT3 pathway reduces gastric cancer growth in vitro and in vivo. *PLoS One.* 2014;9(5):e95993.

SUPPORTING INFORMATION

Additional supporting information can be found online in the Supporting Information section at the end of this article.

How to cite this article: Li H, Liu Y, Liu Y, Xu L, Sun Z, Zheng D, et al. Tumor-associated astrocytes promote tumor progression of Sonic Hedgehog medulloblastoma by secreting lipocalin-2. *Brain Pathology.* 2024;34(1):e13212. <https://doi.org/10.1111/bpa.13212>